

4D Radar-Inertial Odometry based on Gaussian Modeling and Multi-Hypothesis Scan Matching

Fernando Amodeo¹, Luis Merino, *Member, IEEE*¹ and Fernando Caballero¹

Abstract—4D millimeter-wave (mmWave) radars are sensors that provide robustness against adverse weather conditions (rain, snow, fog, etc.), and as such they are increasingly being used for odometry and SLAM applications. However, the noisy and sparse nature of the returned scan data proves to be a challenging obstacle for existing point cloud matching based solutions, especially those originally intended for more accurate sensors such as LiDAR. Inspired by visual odometry research around 3D Gaussian Splatting [10], in this paper we propose using freely positioned 3D Gaussians to create a summarized representation of a radar point cloud tolerant to sensor noise, and subsequently leverage its inherent probability distribution function for registration (similar to NDT [2]). Moreover, we propose simultaneously optimizing multiple scan matching hypotheses in order to further increase the robustness of the system against local optima of the function. Finally, we fuse our Gaussian modeling and scan matching algorithms into an EKF radar-inertial odometry system designed after current best practices. Experiments using publicly available 4D radar datasets show that our Gaussian-based odometry is comparable to existing registration algorithms, outperforming them in several sequences.

Our code and results can be publicly accessed at: <https://github.com/robotics-upo/gaussian-rio-cpp>

I. INTRODUCTION

4D millimeter-wave (mmWave) radars have earned considerable popularity in the world of robotics as an alternative to classic camera or LiDAR sensors due to their robustness against adverse weather conditions (rain, snow, fog, etc.), as well as their compact size and low power consumption. As such, there is considerable interest in incorporating these sensors in odometry and SLAM applications. Existing LiDAR odometry solutions have been applied, adapted and sometimes even further specialized to 4D radar, with varying degrees of success [28], [29], [30], [26], [24]. However, the point clouds generated by 4D radars are sparser, noisier, and have a narrower field of view compared to those generated by LiDARs; and as a result these algorithms often struggle with the geometry of certain scenes. Therefore, it is desirable to explore scene representations that directly model coarse-grained surfaces and regions of radar point clouds instead of focusing on individual points themselves.

Another technique that has gained popularity recently in the field of robotics is 3D Gaussian Splatting (3DGS) [10]. This algorithm creates an explicit representation of a visual scene, and has been applied to SLAM [16], [9], [1] as an alternative to existing methods using implicit representations such as NeRF [17]. However, 3DGS heavily relies on the

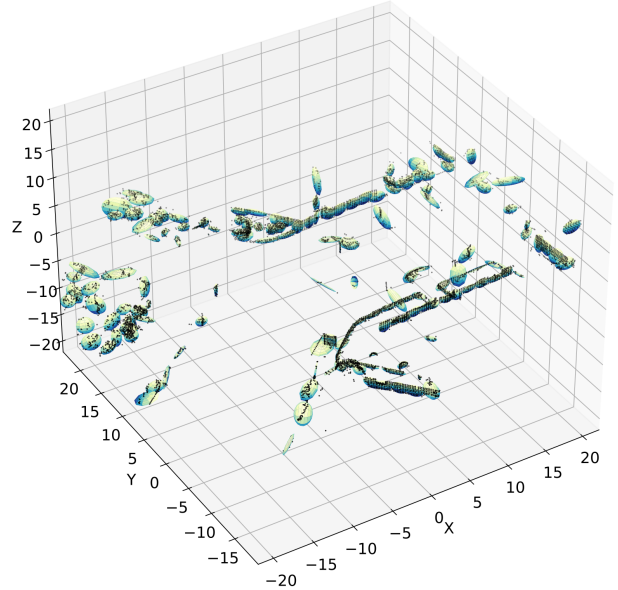


Fig. 1. Gaussian model of an example point cloud, containing 150 Gaussians. The surface of each spheroid represents the 2σ front of each Gaussian (i.e. Mahalanobis distance equal to two).

nature of visual information for training and rendering, and thus adapting it for use with LiDAR or radar instead of visual cameras is challenging; as opposed to NeRF, which can be straightforwardly adapted to model a SDF instead [18].

In this paper we draw inspiration from both lines of research to propose the use of Gaussian models for representing a point cloud and performing registration with respect to it, as an alternative to existing registration methods such as the Normal Distributions Transform (NDT) [2] or Generalized Iterative Closest Point (GICP) [21]. Gaussians are freely positioned in space instead of following a regular grid, as in 3DGS and unlike NDT. Moreover, our scan matching (registration) step considers multiple simultaneous hypotheses, which can in some situations increase the performance of the system, as we show in our experiments. In addition, we outline an Extended Kalman Filter (EKF) based approach to radar-inertial odometry that consolidates existing practices by integrating both radar egovelocidad [4] and keyframing/scan matching components, which we then use to evaluate our Gaussian-based approach in comparison to other registration algorithms on multiple datasets and radar types.

Figure 2 shows the overall pipeline of our odometry system. As in other solutions, we use an Extended Kalman Filter

¹Service Robotics Laboratory – Universidad Pablo de Olavide (Seville), Spain {famozur, lmercab, fcaballero}@upo.es

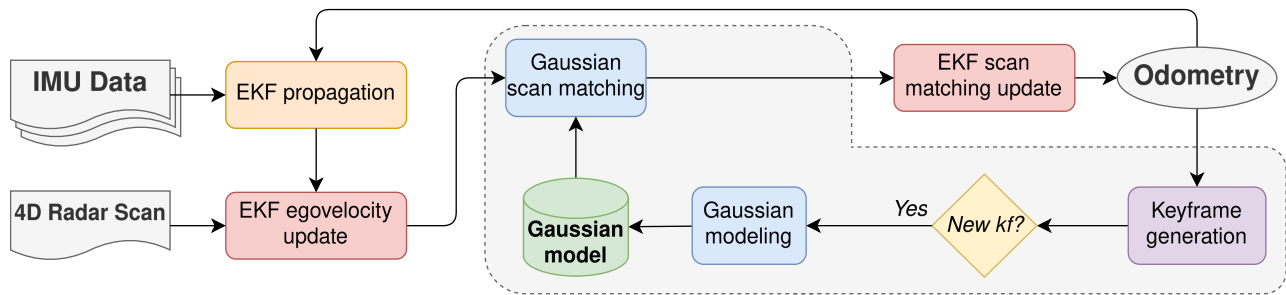


Fig. 2. Overview of the proposed Gaussian radar-inertial odometry pipeline

(EKF) to perform inertial strapdown and process sensory input, including radar egovelocity. Keyframing is used to select individual 4D radar scans, which then undergo Gaussian modeling. The Gaussian multi-hypothesis scan matching algorithm registers every incoming 4D radar scan against the Gaussian model in order to produce a relative pose observation with respect to the last keyframe, which is then used to further update the EKF.

This paper is organized as follows: Section II reviews existing related literature, Sections III, IV and V describe the three main components of our method respectively: Gaussian modeling, Gaussian scan matching, and the Extended Kalman Filter tying everything together; Section VI shows experimental results, and Section VII closes the paper with some conclusions.

II. RELATED WORK

A. Odometry and SLAM

There exist a large number of works focused on odometry, sometimes even attaining a full SLAM pipeline (including loop closure). Particularly we are interested in approaches that use non-visual sensors, such as [27], [25], [19], [4], [5], [28], [29], [30], [26], [24], [31]. These works use a 3D LiDAR or 4D radar sensor, sometimes together with an IMU, to provide an odometry solution. The main technical advantage of these sensors over visual sensors (cameras) is their increased field/depth of view and robustness to adverse environmental conditions: in particular, both are immune to low light conditions, and 4D radar in addition offers robustness to fog, dust and rain. Moreover, 4D radar is uniquely capable of measuring the velocity of objects by leveraging the Doppler effect. Researchers have taken advantage of this to directly measure the robot’s own velocity (“egovelocity”) [4], [5], something which has been shown to significantly improve the performance of odometry systems.

Registration of incoming point clouds with respect to previous ones is a key technique used in some of the cited odometry systems. In particular, the most widely used algorithm for aligning point clouds is Generalized Iterative Closest Point (GICP) [21]. This algorithm calculates distribution probability at each point based on their neighborhood, and optimizes a distribution-to-distribution scan matching function. In the case of radar scans, this is a more difficult task compared to LiDAR because of the lower number and density

of points, as well as higher measurement noise/uncertainty in each point’s position. For this reason [30] proposed the Adaptive Probability Distribution variant of the algorithm (APDGICP), which leverages GICP’s ability to make use of the spatial probability distribution of each point, calculating the required point position covariance matrices according to the radar specifications. However, this is still in essence an approach focused on individual points, without attempting to extract larger scale geometric features that may be more stable and robust for registration purposes.

The works cited in this section use different sources of information, however many do not leverage all mentioned sources at the same time. Table I includes a list of surveyed methods.

B. Gaussian-based modeling

The Normal Distributions Transform (NDT) algorithm [2] slices and subdivides a point cloud using a regular grid and computes normal distributions for each cell that contains points. Scan matching is performed by maximizing the resulting probability distribution function with respect to an incoming scan. An important limitation of this algorithm is the fact that the grid structure itself imposes restrictions on the geometry, and the resulting model may not be fine grained enough to accurately model the geometry of the environment. Another problem lies in the fact that discontinuities in the probability function are produced when partially registered points cross cell boundaries during optimization. Moreover, the original authors only consider 2D scan matching (requiring 3D point clouds to be projected into the XY plane), although subsequent works [15] extend the algorithm to 3D. NDT has been used with radar scans too [13], [14], albeit without inertial information. Another similar algorithm is the Voxelized GICP (VGICP) [12], which also creates an NDT-like voxel-based representation to serve as the reference model, and combines it with the distribution-to-distribution based approach of GICP.

3D Gaussian Splatting (3DGS) [10] is a popular technique for creating a model of a scene from multiple posed images. A 3DGS model is a collection of multiple 3D normal distributions (Gaussians) freely distributed in space, each also containing color/radiance information encoded using spherical harmonics. Even though this technique was originally developed as an alternative to NeRF [17] for novel

view synthesis, researchers have successfully leveraged this representation to develop SLAM solutions [16], [9], [1]. However, 3DGS and these works are all designed for visual sensors (cameras), and they cannot leverage other sensors such as LiDAR or radar due to the nature of the representation. This affects the rendering process in particular: while NeRF’s ray casting framework can be easily adapted to directly predict the output of a SDF [18] (therefore removing the volume rendering component from the system), the differentiable tile rasterizer is a core part of 3DGS that cannot be avoided, neither during training nor inference; thus requiring significant redesign efforts in order to synthesize other types of data such as LiDAR scans [3].

III. GAUSSIAN MODELING

Given a point cloud \mathcal{P} containing M points $\{\mathbf{p}_i | i = 0, 1, \dots, M\}$ with $\mathbf{p}_i \in \mathbb{R}^3$, our goal is creating a summarized representation of its geometry for use with downstream tasks such as mapping or localization. Following the line of works such as NDT [2] and 3DGS [10], we decided to model the geometry using normal distributions. Figure 1 shows an example of a Gaussian model.

A. Parametrization

We parametrize the Gaussian model \mathcal{G} of a scene as a collection of N independent trivariate normal distributions (**3D Gaussians**), each modeling the geometry of an individual region in space. The model is described by the following parameters of each Gaussian $\theta_j = \{\boldsymbol{\mu}_j, \mathbf{s}_j, \mathbf{q}_j\}$:

- Center point $\boldsymbol{\mu}_j \in \mathbb{R}^3$, indicating the mean of the distribution.
- Scaling vector $\mathbf{s}_j \in \mathbb{R}^3$, indicating the natural logarithms of the square roots of the eigenvalues of the covariance matrix. We impose a minimum size restriction so that Gaussians do not become infinitely small (and Mahalanobis distances infinitely large).
- Rotation quaternion $\mathbf{q}_j \in \mathbb{H}$, compactly encoding the eigenvectors of the covariance matrix (see below); where \mathbb{H} is the field of quaternions. In order to ensure that the quaternions remain unitary during the optimization, we normalize them prior to usage.

Unlike in Gaussian Mixture Models (GMMs), we do not define π_j weight parameters for the prior probability of a point being generated by a given Gaussian. This is because point cloud data does not encode a complete population of points – it merely represents a *sample* of said population, biased by factors such as the physical geometric properties of the sensor. For instance, sampling density is inversely proportional to distance from the sensor. This means we cannot model these prior probabilities, and as such we only consider posterior probabilities after a point is assigned to a Gaussian (through other non-probabilistic means, such as measuring distances).

The scaling and rotation parameters succinctly describe the covariance matrix of a normal distribution [23], [6]. To see why this is possible, we first derive a rotation matrix $\mathbf{R}_j = \mathbf{R}\{\mathbf{q}_j\}$, and a scaling matrix $\mathbf{S}_j = \text{diag}(\exp_{\circ}(\mathbf{s}_j))$, where

$\exp_{\circ}(\mathbf{x})$ is element-wise natural exponentiation and $\mathbf{R}\{\mathbf{q}\}$ is the quaternion-to-rotation-matrix conversion operator. We then define a transformation matrix $\mathbf{M}_j = \mathbf{R}_j \mathbf{S}_j$ that maps a mean-centered point into the Gaussian’s correlation space, and finally derive the covariance matrix $\boldsymbol{\Sigma}_j = \mathbf{M}_j \mathbf{M}_j^T$ of the distribution.

B. Initialization

First, it is necessary to determine N , that is, the number of 3D Gaussians in the model. We propose choosing N proportionally based on the number of points, so that richer scans can be represented with more Gaussians. The model \mathcal{G} is then initialized with all \mathbf{s}_j set to 0 (indicating unit scale), and all \mathbf{q}_j set to the unit quaternion. As for $\boldsymbol{\mu}_j$, we perform Bisecting K-Means clustering to find initial estimates for the centers of the Gaussians.

C. Optimization

\mathcal{G} is optimized iteratively using gradient descent. Each epoch involves the following steps:

- Each point of \mathcal{P} is matched to the nearest Gaussian center point $\boldsymbol{\mu}_j$. This process builds a set G_j for each Gaussian, containing all matched points. We use the standard Euclidean distance in this step as opposed to the Mahalanobis distance in order to avoid a feedback loop between center and covariance matrix optimization that results in exploding gradients.
- Each point \mathbf{p}_i is transformed to the coordinate space of its assigned Gaussian as such: $\hat{\mathbf{p}}_i = \mathbf{M}_j^{-1}(\mathbf{p}_i - \boldsymbol{\mu}_j)$. Note that $\mathbf{M}_j^{-1} = \mathbf{S}_j^{-1} \mathbf{R}_j^T$, and \mathbf{S}_j^{-1} is trivial to calculate since \mathbf{S}_j is a diagonal matrix.
- The parameters of \mathcal{G} (in other words, all θ_j) are updated using the gradient of the loss function.

We define the following loss function affecting a given θ_j , derived from the log PDF of the multivariate normal distribution:

$$\mathcal{L}_j = \frac{1}{2|G_j|} \sum_{\mathbf{p}_i \in G_j} \hat{\mathbf{p}}_i^T \hat{\mathbf{p}}_i + \sum_k^3 \mathbf{s}_{j_k}. \quad (1)$$

The loss function \mathcal{L} of the entire model \mathcal{G} can be obtained by taking the mean of the loss values across all Gaussians.

IV. GAUSSIAN MULTI-HYPOTHESIS SCAN MATCHING

Given a Gaussian model \mathcal{G} and a point cloud \mathcal{P} , we define a registration process that estimates the pose of the robot ξ with respect to \mathcal{G} . The algorithm is based on the simultaneous optimization of multiple hypotheses centered around the current predicted position of the robot, in order to increase the robustness against local optima.

A. Definitions

We define the robot pose ξ to be a member of $SE(3)$; that is, it includes a translational component $\mathbf{t} \in \mathbb{R}^3$ and rotational component $\mathbf{q} \in SO(3)$, with respect to *some* frame of reference. We consider that the uncertainty about the true robot pose follows *some* probability distribution: $\xi \sim P$.

Given a suitable model of \mathcal{P} , we can randomly sample a swarm of K pose particles $\hat{\xi}^k$, each representing a different hypothesis, and use an optimization algorithm that evaluates each particle against \mathcal{G} to further refine these estimates until one of the particles reaches a suitable optimum. We believe exploring the solution space using a particle swarm increases robustness in challenging situations, especially when dealing with large rotations or translations.

B. Optimization

The process is performed iteratively using Gauss-Newton. Each iteration involves the following steps:

- We define K virtual copies of \mathcal{P} called $\mathcal{P}^{/k}$, each registered according to every pose hypothesis $\hat{\xi}^k$.
- Every point \mathbf{p}_i^k of $\mathcal{P}^{/k}$ is matched to the Gaussian θ_j in \mathcal{G} that results in the lowest Mahalanobis distance, which we call d_i^k .
- We perform the usual Gauss-Newton update step for each particle $\hat{\xi}^k$, using the sums of squared Mahalanobis distances as the function to optimize, as in GICP. We also exclude points whose d_i^k is greater than a given distance threshold d_{\max} .

The optimization stops when all particles converge to a solution (i.e. when the update applied is under a given order of magnitude), or when a maximum number of iterations is reached; whichever happens first. The resulting output pose of the registration algorithm is the particle with the lowest value of the scoring function \mathcal{L}_k defined as follows:

$$\mathcal{L}_k = \frac{1}{M} \sum_i^M \min(d_i^k, d_{\max}), \quad (2)$$

where M is the number of points in the scan. We consider a failure condition when the output particle has not converged.

C. Keyframing

A common technique used in odometry systems is keyframing. Certain poses of the robot are selected to become local reference points (keyframes) that are later used for registration, graph optimization or loop closure purposes. In our case, we use keyframing to select individual radar point clouds to undergo Gaussian modeling, and serve as reference for Gaussian scan matching of subsequent radar point clouds. This has the benefit of reducing the accumulated error that arises from successive applications of the scan matching algorithm, though it also means the criteria used to select keyframe candidates needs to be carefully designed to generate the appropriate keyframe pacing. We use a simple set of criteria to decide when a new pose ξ^j qualifies to become a new keyframe. Given the most recent keyframe ξ^i , we can derive the $SE(3)$ transformation relative to the keyframe $T = \xi^j \ominus \xi^i = \{\mathbf{t}, \mathbf{q}\}$. The criteria are then simply that any of the following must hold:

- For the translational component: $\|\mathbf{t}\|_2 \geq d_{\max}$, where d_{\max} is the maximum distance threshold.
- For the rotational component: $2 \cos^{-1} |q_w| \geq \alpha_{\max}$, where α_{\max} is the maximum rotation angle threshold.

As a fallback, if no scans have returned a successful match during the past given time interval t , a keyframe is automatically generated.

V. INERTIAL ODOMETRY WITH EKF

We use an Extended Kalman Filter in our odometry solution to tightly integrate all incoming sensor information: inertial data, radar egovelocity observations, and scan matching results. Unlike other published solutions [22], [4], [5], we only use Error State filtering for rotational variables, as opposed to the entire state. We employ the right-handed North-West-Up (NWU) convention typical of robotics, and consider three reference frames: world (w), body/IMU (b) and radar (r). The rotation matrix \mathbf{C}_f^g transforms a vector from frame f to frame g , likewise $\mathbf{C}_g^f = (\mathbf{C}_f^g)^T$. We decompose each \mathbf{C} into an error part and a nominal quaternion part as follows: $\mathbf{C} = \exp([\delta\theta]_{\times}) \mathbf{R}\{\mathbf{q}\}$, approximating the error part as $\mathbf{I} + [\delta\theta]_{\times}$ for the purposes of linearization.

The state (\mathbf{x}), control (\mathbf{u}) and noise (\mathbf{w}) vectors of the filter are the following:

$$\mathbf{x} = \begin{bmatrix} \mathbf{p} \\ \mathbf{v} \\ \mathbf{t}_r^b \\ \mathbf{b}_a \\ \mathbf{b}_\omega \\ \delta\theta_b^w \\ \delta\theta_r^b \end{bmatrix}; \quad \mathbf{u} = \begin{bmatrix} \mathbf{a} \\ \boldsymbol{\omega} \end{bmatrix}; \quad \mathbf{w} = \begin{bmatrix} \mathbf{w}_v \\ \mathbf{w}_\theta \\ \mathbf{w}_a \\ \mathbf{w}_\omega \\ \mathbf{w}_{b_a} \\ \mathbf{w}_{b_\omega} \end{bmatrix}, \quad (3)$$

where \mathbf{p} is the position, \mathbf{v} is the velocity, \mathbf{t}_r^b is the translation between radar and IMU, \mathbf{b}_a and \mathbf{b}_ω are the accelerometer/gyroscope biases, each $\delta\theta$ is the error part of its corresponding \mathbf{C} frame expressed as a tangential rotation $\in \mathfrak{so}(3)$, and \mathbf{a} and $\boldsymbol{\omega}$ are the IMU accelerometer/gyroscope readings. The position and velocity of the robot are expressed in the world frame, while the nominal rotations \mathbf{q}_b^w and \mathbf{q}_r^b are stored outside the filter state as quaternions. Velocity and attitude process noise are modeled by \mathbf{w}_v and \mathbf{w}_θ respectively. We follow Kalibr's IMU noise model [20]¹, and consider both additive ($\mathbf{w}_a, \mathbf{w}_\omega$) and random walk noise ($\mathbf{w}_{b_a}, \mathbf{w}_{b_\omega}$) in accelerometer/gyroscope readings.

There also exists a vector $\mathbf{g} = -[0 \ 0 \ 9.80511]^T$ modeling the Earth's gravity treated as a constant, as we do not consider long enough travel distances for changes in the plane tangent to the Earth's surface to matter.

A. EKF initialization

First, we initialize all components of the state vector \mathbf{x} to 0, and the rotational variables to the unit quaternion. The initial radar-to-IMU frame ($\mathbf{t}_r^b, \mathbf{q}_r^b$) can be supplied externally. The robot is assumed to remain still during the first few seconds, which allows for averaging initial accelerometer/gyroscope readings and extracting an estimate of the body-frame gravity vector $\tilde{\mathbf{g}}_b$ (after flipping sign) and the gyroscope bias \mathbf{b}_ω respectively. An initial value for the roll/pitch components of \mathbf{q}_b^w can then be derived from $\tilde{\mathbf{g}}_b$,

¹<https://github.com/ethz-asl/kalibr/wiki/IMU-Noise-Model>

while the yaw component is set to 0 since we are not incorporating a compass/magnetometer. In addition, we derive the initial accelerometer bias as $\mathbf{b}_a = \mathbf{C}_w^b (\mathbf{C}_b^w \hat{\mathbf{g}}_b - \mathbf{g})$, thus taking into account the difference in magnitude between the expected and observed gravity vectors.

We initialize the covariance matrix mostly as 0, except for the subblocks related to \mathbf{t}_r^b , \mathbf{b}_a , \mathbf{b}_ω , $\delta\theta_b^w$ and $\delta\theta_r^b$, whose diagonals we fill in according to supplied initial values.

B. EKF propagation

We use a simplified inertial strapdown formulation that assumes movement to be linear instead of being perturbed by the current angular velocity reading of the gyroscope, due to the short time interval and small change in attitude (in effect equivalent to first order integration):

$$\mathbf{p} \leftarrow \mathbf{p} + \mathbf{v}t + \frac{1}{2}(\mathbf{C}_b^w(\mathbf{a} - \mathbf{b}_a) + \mathbf{g})t^2, \quad (4)$$

$$\mathbf{v} \leftarrow \mathbf{v} + (\mathbf{C}_b^w(\mathbf{a} - \mathbf{b}_a) + \mathbf{g})t, \quad (5)$$

$$\mathbf{q} \leftarrow \mathbf{q} \otimes \exp\left(\frac{1}{2}(\boldsymbol{\omega} - \mathbf{b}_\omega)t\right). \quad (6)$$

The strapdown formulation is linearized in order to propagate the covariance matrix:

$$\mathbf{P} \leftarrow \mathbf{F}\mathbf{P}\mathbf{F}^T + \mathbf{N}\mathbf{Q}\mathbf{N}^T, \quad (7)$$

where \mathbf{F} is the linearized state transition matrix, \mathbf{Q} is the noise covariance matrix, and \mathbf{N} is the noise state transition matrix. These three matrices are sparsely populated: $\mathbf{F} = \mathbf{I}$ and $\mathbf{Q} = \mathbf{N} = \mathbf{0}$, except for the following subblocks:

$$\mathbf{F}_{pv} = \mathbf{I}t; \mathbf{F}_{pb_a} = -\frac{1}{2}\mathbf{C}_b^w t^2; \mathbf{F}_{p\delta\theta_b^w} = -\frac{1}{2}[\mathbf{C}_b^w \mathbf{a}]_{\times} t^2; \quad (8)$$

$$\mathbf{F}_{vb_a} = \mathbf{F}_{\delta\theta_b^w b_\omega} = -\mathbf{C}_b^w t; \mathbf{F}_{v\delta\theta_b^w} = -[\mathbf{C}_b^w \mathbf{a}]_{\times} t; \quad (9)$$

$$\mathbf{Q}_{vv} = \mathbf{I}\sigma_v^2; \mathbf{Q}_{\theta\theta} = \mathbf{I}\sigma_\theta^2; \mathbf{Q}_{aa} = \mathbf{I}\frac{\sigma_a^2}{t}; \quad (10)$$

$$\mathbf{Q}_{\omega\omega} = \mathbf{I}\frac{\sigma_\omega^2}{t}; \mathbf{Q}_{b_a b_a} = \mathbf{I}\sigma_{b_a}^2; \mathbf{Q}_{b_\omega b_\omega} = \mathbf{I}\sigma_{b_\omega}^2 t; \quad (11)$$

$$\mathbf{N}_{pa} = \frac{1}{2}\mathbf{C}_b^w t^2; \mathbf{N}_{va} = \mathbf{N}_{\delta\theta_b^w \omega} = \mathbf{C}_b^w t; \quad (12)$$

$$\mathbf{N}_{vv} = \mathbf{N}_{\delta\theta_b^w \theta} = \mathbf{N}_{b_a b_a} = \mathbf{N}_{b_\omega b_\omega} = \mathbf{I}, \quad (13)$$

where σ_v , σ_θ , σ_a , σ_ω , σ_{b_a} and σ_{b_ω} are the standard deviations of the respective components of \mathbf{w} .

C. EKF update and error state reset

Given observation \mathbf{y} , residual observation vector \mathbf{r} , observation covariance matrix \mathbf{R} and linearized observation matrix \mathbf{H} (so that $\mathbf{r} \approx \mathbf{y} - \mathbf{H}\mathbf{x}$), we can proceed to apply the Kalman filter equations (in Joseph form):

$$\mathbf{K} = \mathbf{P}\mathbf{H}^T(\mathbf{H}\mathbf{P}\mathbf{H}^T + \mathbf{R})^{-1}; \mathbf{L} = \mathbf{I} - \mathbf{K}\mathbf{H}, \quad (14)$$

$$\mathbf{x} \leftarrow \mathbf{x} + \mathbf{K}\mathbf{r}; \mathbf{P} \leftarrow \mathbf{L}\mathbf{P}\mathbf{L}^T + \mathbf{K}\mathbf{R}\mathbf{K}^T. \quad (15)$$

As previously mentioned, rotations are expressed as error state in the EKF, and after an EKF update the nominal

value of each $\delta\theta$ becomes non-zero, making it necessary to incorporate the estimated error back into the state as follows:

$$\mathbf{q} \leftarrow \delta\mathbf{q} \otimes \mathbf{q}; \delta\mathbf{q} = \exp\left(\frac{1}{2}\delta\boldsymbol{\theta}\right), \quad (16)$$

$$\delta\boldsymbol{\theta} \leftarrow \mathbf{0}; \mathbf{P} \leftarrow \mathbf{G}\mathbf{P}\mathbf{G}^T; \mathbf{G}_{\delta\theta\delta\theta} = \mathbf{R}\{\delta\mathbf{q}\}, \quad (17)$$

where \mathbf{G} is the error reset matrix, and it is a sparse matrix equal to \mathbf{I} except for every $\delta\theta\delta\theta$ subblock.

Finally, in order to prevent especially noisy observations from causing instability in the filter, we perform Mahalanobis outlier rejection, using a threshold calculated from a given percentile of the χ^2 distribution, like [4].

D. Radar egovelocity observation

Following previous works, we directly observe the robot's velocity by leveraging the Doppler effect in measurements returned by the radar. We use the RANSAC-LSQ algorithm [4] to both filter out outlier (dynamic) points, and estimate the current radar-frame velocity of the robot, including a covariance matrix. The filtered point cloud is also fed to the Gaussian modeling and scan matching algorithm in the following subsection. The observation model used to perform the EKF update is as follows:

$$\mathbf{r} = \mathbf{y} - \mathbf{C}_b^r([\boldsymbol{\omega}]_{\times}\mathbf{t}_r^b + \mathbf{C}_w^b\mathbf{v}); \quad (18)$$

$$\mathbf{H}_{:v} = \mathbf{C}_b^r\mathbf{C}_w^b; \mathbf{H}_{:t_r^b} = \mathbf{C}_b^r[\boldsymbol{\omega}]_{\times}; \mathbf{H}_{:b_\omega} = \mathbf{C}_b^r[\mathbf{t}_r^b]_{\times}; \quad (19)$$

$$\mathbf{H}_{:\delta\theta_b^w} = \mathbf{C}_b^r\mathbf{C}_w^b[\mathbf{v}]_{\times}; \mathbf{H}_{:\delta\theta_r^b} = \mathbf{C}_b^r([\boldsymbol{\omega}]_{\times}\mathbf{t}_r^b + \mathbf{C}_w^b\mathbf{v})_{\times}. \quad (20)$$

E. Scan matching observation

The Gaussian modeling and scan matching algorithms allow us to observe robot poses relative to previous keyframes. In other words, given a keyframe pose ξ^k we can observe the change in translation and rotation that has occurred since said keyframe. We initialize the pose particle swarm with a distribution $\mathbf{P} \sim \mathcal{N}(\xi^x, \boldsymbol{\Sigma})$ where ξ^x is the relative robot pose formed from the current nominal state of the EKF: $\xi^x = \{\mathbf{p}, \mathbf{q}\} \ominus \xi^k$, and $\boldsymbol{\Sigma}$ is a covariance matrix indicating the desired dispersion of the particles for each of the 6 degrees of freedom (X/Y/Z/roll/pitch/yaw). Afterwards, we apply the scan matching algorithm and obtain an optimized observation pose ξ^y , from which a residual pose can be obtained: $\xi^r = \xi^y \ominus \xi^x = \{\delta\mathbf{p}, \delta\mathbf{q}\}$. Since the attitude error quaternion $\delta\mathbf{q}$ can be approximated as $\delta\mathbf{q} = \exp\left(\frac{1}{2}\delta\boldsymbol{\theta}\right) \approx [1 \frac{1}{2}\delta\boldsymbol{\theta}^T]^T$ for very small errors, the attitude error vector can be approximated as $\delta\boldsymbol{\theta} \approx \frac{2}{\delta q_w}\delta\mathbf{q}_v$. This allows us to construct the residual vector $\mathbf{r} = [\delta\mathbf{p}^T \delta\boldsymbol{\theta}^T]^T$ to be fed to the EKF update equation – note that this vector contains X/Y/Z/roll/pitch/yaw components (in this order). The non-zero subblocks of the observation matrix \mathbf{H} can be defined as such: $\mathbf{H}_{\delta p p} = \mathbf{H}_{\delta\theta\delta\theta} = \mathbf{C}_w^k$, where k corresponds to the keyframe's reference frame. We are currently using a fixed observation covariance matrix \mathbf{R} , although we believe it should be possible to leverage the optimized particle swarm

TABLE I
RESULTS ON NTU4DRadLM DATASET (OCULII EAGLE). BEST RESULTS IN **BOLD**, SECOND BEST RESULTS UNDERLINED.
METHODS MARKED WITH * ARE SELF-REPORTED METRICS. EV: EGOVELOCITY, SM: SCAN MATCHING

	Usage			cp		nyl		loop2		loop3	
	IMU	EV	SM	t_{rel} (%)	r_{rel} (%/m)	t_{rel} (%)	r_{rel} (%/m)	t_{rel} (%)	r_{rel} (%/m)	t_{rel} (%)	r_{rel} (%/m)
<i>NTU4DRadLM baseline: gicp*</i> [29]	–	✓	✓	4.13	0.0552	4.62	0.0184	4.84	0.0060	3.22	0.0060
<i>NTU4DRadLM baseline: Fast-LIO*</i> [29]	✓	–	✓	2.94	0.0468	3.80	0.0208	7.16	0.0057	4.55	0.0064
<i>4DRadarSLAM apdgicp*</i> [30]	–	✓	✓	3.56	0.0369	3.55	0.0171	6.09	0.0082	4.09	0.0097
<i>EFEAR-4D*</i> [26]	–	✓	✓	5.09	0.0125	8.93	0.0166	37.27	0.0152	37.01	0.0175
<i>RIV-SLAM*</i> [24]	✓	✓	✓	2.58	0.0342	–	–	2.69	0.0456	–	–
EKF-RIO [4]	✓	✓	–	14.76	0.3955	35.89	0.2464	44.31	0.0349	50.23	0.0910
(Ablation) Our EKF with NDT [2]	✓	✓	✓	2.42	0.0345	7.80	0.0408	5.61	0.0065	7.84	0.0100
(Ablation) Our EKF with GICP [21]	✓	✓	✓	2.93	0.0428	2.97	0.0111	2.99	0.0038	<u>3.50</u>	<u>0.0042</u>
(Ablation) Our EKF with VGICP [12]	✓	✓	✓	2.43	0.0362	2.56	0.0136	2.73	<u>0.0036</u>	3.84	0.0047
(Ablation) Gaussian single hypothesis	✓	✓	✓	<u>2.15</u>	0.0318	<u>2.46</u>	<u>0.0116</u>	2.44	0.0030	3.97	0.0043
Gaussian multi-hypothesis	✓	✓	✓	1.64	<u>0.0310</u>	2.41	0.0117	<u>2.61</u>	<u>0.0036</u>	3.71	0.0040

TABLE II
RESULTS ON SNAIL-RADAR DATASET (OCULII EAGLE). BEST RESULTS IN **BOLD**, SECOND BEST RESULTS UNDERLINED.

	st_20231213_1		iaf_20231213_2		iaf_20231213_3		if_20231213_4		if_20231213_5	
	t_{rel} (%)	r_{rel} (mrad/m)								
(Ablation) Our EKF with NDT [2]	4.13	0.5286	2.04	0.0519	3.95	0.0653	2.86	0.0786	3.15	0.0771
(Ablation) Our EKF with GICP [21]	3.77	0.5118	2.93	0.0629	4.05	0.0629	2.77	0.1136	4.58	0.1572
(Ablation) Our EKF with VGICP [12]	3.68	<u>0.5141</u>	3.06	0.0610	3.17	0.0551	2.53	0.1167	4.44	0.1489
(Ablation) Gaussian single hypothesis	<u>3.36</u>	<u>0.5204</u>	2.85	0.0689	2.84	<u>0.0537</u>	2.36	<u>0.0927</u>	<u>4.00</u>	<u>0.1457</u>
Gaussian multi-hypothesis	3.33	0.5147	<u>2.45</u>	<u>0.0543</u>	<u>2.89</u>	0.0498	<u>2.55</u>	0.1093	4.32	0.1569

TABLE III
RESULTS ON SNAIL-RADAR DATASET (ARS548). BEST RESULTS IN **BOLD**, SECOND BEST RESULTS UNDERLINED.

	st_20231213_1		iaf_20231213_2		iaf_20231213_3		if_20231213_4		if_20231213_5	
	t_{rel} (%)	r_{rel} (mrad/m)								
(Ablation) Our EKF with GICP [21]	1.69	0.3049	3.36	0.0507	3.29	0.0487	2.42	0.0761	2.26	0.0796
(Ablation) Our EKF with VGICP [12]	1.95	0.2798	2.57	0.0494	3.10	0.0491	2.81	0.0777	2.12	0.0836
(Ablation) Gaussian single hypothesis	1.34	0.3727	2.50	0.0487	2.77	0.0475	<u>2.47</u>	0.0826	2.37	0.0740
Gaussian multi-hypothesis	<u>1.60</u>	0.3573	4.02	0.0756	6.80	0.1000	2.93	0.0894	<u>2.25</u>	<u>0.0746</u>

returned by the scan matching algorithm to estimate this matrix.

Furthermore, we constrain the observation model described above by removing degrees of freedom that are deemed noisy in the scan matching due to the properties of the sensor. For example, radars have lower resolution in the Z axis, which degrades the usefulness of Z/roll/pitch information returned by scan matching algorithms. In order to ignore the unreliable degrees of freedom, we transform the residual vector, observation matrix and covariance matrix by removing the rows and/or columns corresponding to Z/roll/pitch prior to applying the EKF update.

VI. EXPERIMENTAL RESULTS

In order to evaluate the performance of our Gaussian modeling and scan matching method, we use existing public 4D radar datasets. In particular, we selected the NTU4DRadLM [29] and Snail-Radar [8] datasets, because together they cover multiple radar types (Oculii Eagle and ARS548),

multiple robot platform types (handcart and car), and adverse conditions.

We evaluate relative translation/rotation errors using the modern and flexible evo evaluation package [7], while preserving existing practice by using a custom evaluation script that follows the behavior of older packages such as `rpg_trajectory_evaluation` as closely as possible. In the case of Snail-Radar sequences, we report rotation errors in mrad/m instead of %/m because the errors are much smaller.

Besides our full method, we evaluate four ablations within our EKF framework: one without multi-hypothesis registration, and three replacing our Gaussian-based algorithms with NDT, GICP and VGICP. Since these are all single-hypothesis methods, we use the current nominal state of the EKF directly as the initial estimate (instead of sampling a random particle swarm). The NDT version uses the implementation provided by the well known PCL (Point Cloud Library), while the GICP and VGICP versions use `small_gicp` [11] as the underlying implementation. In the case of Oculii Eagle scans,

we set a target of 20 points per Gaussian; while for ARS548 scans, due to the much lower number of returned points, we set a target of 8 points per Gaussian. In both cases we sample a swarm of 8 particles during scan matching.

The source code of our odometry solution can be accessed online on GitHub². We include the script used to generate the odometry trajectories, and the script used to evaluate trajectories with *evo*. The code also contains all details regarding the system parameters we used, such as EKF covariance initialization, IMU/noise parameters, etc.

A. Results on NTU4DRadLM

We compare our odometry with previous published results on the NTU4DRadLM dataset [29], which includes scans captured by an Oculii Eagle radar, and a VectorNav VN-100 IMU. These include the GICP and Fast-LIO baselines tested in the original NTU4DRadLM paper, the APDGICP algorithm tested in the follow-up 4DRadarSLAM paper [30], as well as other works such as EFEAR-4D [26] or RIV-SLAM [24]. We include these self-reported metrics as-is, as the trajectory files needed for metric calculation are usually not made public. Even though there are no published results for EKF-RIO [4] on this dataset, it is one of the few methods with available source code, and so we are able to produce and include evaluation results for it. We report metrics without loop closure whenever possible, in order to focus on evaluating pure odometry.

We evaluate the *cp*, *ny1* (low speed handcart), *loop2* and *loop3* (high speed car) sequences. The *garden* and *loop1* sequences are excluded because they contain large gaps in the IMU and radar data, respectively.

Table I shows the comparison between all methods. We can observe how our Gaussian methods provide the best or second best results for all sequences except for *loop3*, which seems to favor GICP-based methods (both baseline and our implementation). Moreover, in 3 out of the 4 sequences the multi-hypothesis scan matching approach provides improvements in translation error, especially in *cp*.

B. Results on Snail-Radar

In addition to NTU4DRadLM, we perform additional testing on the Snail-Radar dataset [8], which uses both Oculii Eagle and ARS548 radars together with an Xsens MTi-3-DK IMU, and includes sequences recorded in harsher environment conditions. In particular, we selected the five sequences recorded on 2023/12/13 because of the nighttime and rain conditions of that day under a high speed car platform. These sequences are all fairly long, with the longest (*iaf_20231213_2*) being 15 min and most being around 7 min in length.

Table II shows results using the Oculii Eagle radar. In general, we can observe the best results to be spread across the different methods. Nonetheless, our Gaussian algorithms obtain the best or second best results in 9 out of 10 metrics, and the best translation error in 3 out of 5 sequences (the

other two favoring NDT). The multi-hypothesis approach improves or matches results compared to the single hypothesis version in 3 out of 5 sequences. It is worth mentioning that NDT, unlike in NTU4DRadLM, seems to behave much better in Snail-Radar.

Table III shows results using the ARS548 radar. This radar produces much sparser point clouds than Oculii Eagle (around 10x fewer points). We believe this to be caused by the radar lacking the scan enhancement algorithm used by Oculii Eagle. However interestingly, we can observe better metrics in general compared to Oculii Eagle. The sparser scans trigger a known issue in PCL’s implementation of NDT that cause the program to abnormally terminate, so unfortunately NDT is excluded from the comparison. The results once again show different methods leading in different sequences, however it is worth pointing out that 6 out of the 10 best results are now obtained by our Gaussian algorithms, as well as 3 out of the 10 second best results. Another thing to mention is that the multi-hypothesis scan matching seems to perform worse than the single-hypothesis version. We hypothesize this to be related to the increased sparsity of the scans, and believe it could be solved by improving the sampling distribution of the particles.

C. Summary of results

We consider that the results described above validate our methodology. Our Gaussian modeling and scan matching algorithm produces comparable relative translation and rotation metrics to existing registration algorithms, as shown by the experiments. Moreover, in several sequences across several datasets and radar types our algorithm produces the best overall results. Our EKF-based radar-inertial framework is also validated by the experiments, which show how on a publicly evaluated dataset we are able to improve on the state of the art even when not using our Gaussian algorithms. On the other hand, the multi-hypothesis approach seems to need further adjustments, although it is already capable of producing better results for some sequences.

As an additional observation, it is worth mentioning that we believe the radar-to-IMU calibration file provided by NTU4DRadLM to be inaccurate, as it does not seem to match the placement of the different sensors in the photo they provide of their platform. The effects of this inaccurate calibration can be especially seen in the rotational errors, which are much higher for all methods compared to those achieved under Snail-Radar sequences.

VII. CONCLUSION

In this paper we introduce a Gaussian-based radar-inertial odometry pipeline. Our methods summarize noisy 4D radar scans using freely positioned 3D Gaussians (like 3DGS [10] and unlike NDT [2]), which then support multi-hypothesis scan matching for increased robustness. Through experiments in multiple datasets with multiple radar types, we show that these methods produce results comparable to existing registration algorithms, and even manage to outperform them in several sequences.

²<https://github.com/robotics-upo/gaussian-rio-cpp>

Future works include improving the Gaussian models with an optimization algorithm more efficient than gradient descent, better initialization and dynamic management of Gaussians (as in 3DGS), as well as incorporating radar-specific information such as intensity values; improving the robustness of the multi-hypothesis particle system with kinematic priors, dynamically adjusting the hyperparameters of the system, improving the quality of egoveLOCITY estimation by modeling kinematic restrictions relevant to the robot platform used, further refining the pose estimates by means of Pose Graph Optimization (PGO), incorporating a loop closure module, and creating a global Gaussian map of the environment for the purposes of full SLAM.

ACKNOWLEDGMENT

This work was partially supported by the following grants: 1) INSERTION PID2021-127648OB-C31, and 2) NOR-DIC TED2021-132476B-I00 projects, funded by MCIN/AEI/10.13039/501100011033 and the “European Union NextGenerationEU / PRTR”.

REFERENCES

- [1] Anonymous, “Gaussian-SLAM: Photo-realistic Dense SLAM with Gaussian Splatting,” *Submitted to Transactions on Machine Learning Research*, 2024, under review. [Online]. Available: <https://openreview.net/forum?id=sbkKi8snqH>
- [2] P. Biber and W. Strasser, “The normal distributions transform: a new approach to laser scan matching,” in *Proceedings 2003 IEEE/RSJ International Conference on Intelligent Robots and Systems (IROS 2003) (Cat. No.03CH37453)*, vol. 3, 2003, pp. 2743–2748 vol.3.
- [3] Q. Chen, S. Yang, S. Du, T. Tang, P. Chen, and Y. Huo, “LiDAR-GS: Real-time LiDAR Re-Simulation using Gaussian Splatting,” *arXiv preprint arXiv:2410.05111*, 2024.
- [4] C. Doer and G. F. Trommer, “An EKF Based Approach to Radar Inertial Odometry,” in *2020 IEEE International Conference on Multi-sensor Fusion and Integration for Intelligent Systems (MFI)*, 2020, pp. 152–159.
- [5] —, “Radar Inertial Odometry with Online Calibration,” in *2020 European Navigation Conference (ENC)*, 2020, pp. 1–10.
- [6] P.-E. Forssén, “Low and Medium Level Vision using Channel Representations,” Ph.D. dissertation, Linköping University, Sweden, SE-581 83 Linköping, Sweden, March 2004, appendix C, Dissertation No. 858, ISBN 91-7373-876-X.
- [7] M. Grupp, “evo: Python package for the evaluation of odometry and SLAM.” <https://github.com/MichaelGrupp/evo>, 2017.
- [8] J. Huai, B. Wang, Y. Zhuang, Y. Chen, Q. Li, and Y. Han, “SNAIL radar: A large-scale diverse benchmark for evaluating 4D-radar-based SLAM,” *The International Journal of Robotics Research*, vol. 0, no. 0, p. 02783649251329048, 0. [Online]. Available: <https://journals.sagepub.com/doi/abs/10.1177/02783649251329048>
- [9] N. Keetha, J. Karhade, K. M. Jatavallabhula, G. Yang, S. Scherer, D. Ramanan, and J. Luiten, “SplaTAM: Splat Track & Map 3D Gaussians for Dense RGB-D SLAM,” in *Proceedings of the IEEE/CVF Conference on Computer Vision and Pattern Recognition (CVPR)*, June 2024, pp. 21 357–21 366.
- [10] B. Kerbl, G. Kopanas, T. Leimkühler, and G. Drettakis, “3D Gaussian Splatting for Real-Time Radiance Field Rendering,” *ACM Transactions on Graphics*, vol. 42, no. 4, July 2023. [Online]. Available: <https://repo-sam.inria.fr/fungraph/3d-gaussian-splatting/>
- [11] K. Koide, “small_gicp: Efficient and parallel algorithms for point cloud registration,” *Journal of Open Source Software*, vol. 9, no. 100, p. 6948, Aug. 2024.
- [12] K. Koide, M. Yokozuka, S. Oishi, and A. Banno, “Voxelized GICP for Fast and Accurate 3D Point Cloud Registration,” in *2021 IEEE International Conference on Robotics and Automation (ICRA)*, 2021, pp. 11 054–11 059.
- [13] P.-C. Kung, C.-C. Wang, and W.-C. Lin, “A Normal Distribution Transform-Based Radar Odometry Designed For Scanning and Automotive Radars,” in *2021 IEEE International Conference on Robotics and Automation (ICRA)*, 2021, pp. 14 417–14 423.
- [14] X. Li, H. Zhang, and W. Chen, “4D Radar-Based Pose Graph SLAM With Ego-Velocity Pre-Integration Factor,” *IEEE Robotics and Automation Letters*, vol. 8, no. 8, pp. 5124–5131, 2023.
- [15] M. Magnusson, “The Three-Dimensional Normal-Distributions Transform — an Efficient Representation for Registration, Surface Analysis, and Loop Detection,” Ph.D. dissertation, Örebro University, December 2009.
- [16] H. Matsuki, R. Murai, P. H. Kelly, and A. J. Davison, “Gaussian Splatting SLAM,” in *Proceedings of the IEEE/CVF Conference on Computer Vision and Pattern Recognition (CVPR)*, June 2024, pp. 18 039–18 048.
- [17] B. Mildenhall, P. P. Srinivasan, M. Tancik, J. T. Barron, R. Ramamoorthi, and R. Ng, “NeRF: Representing Scenes as Neural Radiance Fields for View Synthesis,” in *ECCV*, 2020.
- [18] J. Ortiz, A. Clegg, J. Dong, E. Sucar, D. Novotny, M. Zollhoefer, and M. Mukadam, “iSDF: Real-Time Neural Signed Distance Fields for Robot Perception,” in *Robotics: Science and Systems*, 2022.
- [19] P. Pfreundschuh, H. Oleynikova, C. Cadena, R. Siegwart, and O. Andersson, “COIN-LIO: Complementary Intensity-Augmented LiDAR Inertial Odometry,” in *2024 IEEE International Conference on Robotics and Automation (ICRA)*. IEEE, 2024, pp. 1730–1737.
- [20] J. Rehder, J. Nikolic, T. Schneider, T. Hinzmann, and R. Siegwart, “Extending kalibr: Calibrating the extrinsics of multiple IMUs and of individual axes,” in *2016 IEEE International Conference on Robotics and Automation (ICRA)*, 2016, pp. 4304–4311.
- [21] A. Segal, D. Hähnel, and S. Thrun, “Generalized-ICP,” in *Robotics: Science and Systems*. The MIT Press, 2009.
- [22] J. Solà, “Quaternion kinematics for the error-state Kalman filter,” 2017. [Online]. Available: <https://arxiv.org/abs/1711.02508>
- [23] V. Spruyt, “A geometric interpretation of the covariance matrix,” May 2021, accessed: December 2024. [Online]. Available: <https://www.visiondummy.com/2014/04/geometric-interpretation-covariance-matrix/>
- [24] D. Wang, S. May, and A. Nuechter, “RIV-SLAM: Radar-Inertial-Velocity optimization based graph SLAM,” in *2024 IEEE 20th International Conference on Automation Science and Engineering (CASE)*, 2024, pp. 774–781.
- [25] H. Wang, C. Wang, C. Chen, and L. Xie, “F-LOAM: Fast LiDAR Odometry and Mapping,” in *2021 IEEE/RSJ International Conference on Intelligent Robots and Systems (IROS)*, 2020.
- [26] X. Wu, Y. Chen, Z. Li, Z. Hong, and L. Hu, “EFEAR-4D: Ego-Velocity Filtering for Efficient and Accurate 4D radar Odometry,” 2024. [Online]. Available: <https://arxiv.org/abs/2405.09780>
- [27] J. Zhang and S. Singh, “LOAM: Lidar Odometry and Mapping in Real-time,” in *Robotics: Science and Systems*, 07 2014.
- [28] J. Zhang, R. Xiao, H. Li, Y. Liu, X. Suo, C. Hong, Z. Lin, and D. Wang, “4DRT-SLAM: Robust SLAM in Smoke Environments using 4D Radar and Thermal Camera based on Dense Deep Learnt Features,” in *2023 IEEE International Conference on Cybernetics and Intelligent Systems (CIS) and IEEE Conference on Robotics, Automation and Mechatronics (RAM)*, 2023, pp. 19–24.
- [29] J. Zhang, H. Zhuge, Y. Liu, G. Peng, Z. Wu, H. Zhang, Q. Lyu, H. Li, C. Zhao, D. Kircali, S. Mharolkar, X. Yang, S. Yi, Y. Wang, and D. Wang, “NTU4DRadLM: 4D Radar-Centric Multi-Modal Dataset for Localization and Mapping,” in *2023 IEEE 26th International Conference on Intelligent Transportation Systems (ITSC)*, 2023, pp. 4291–4296.
- [30] J. Zhang, H. Zhuge, Z. Wu, G. Peng, M. Wen, Y. Liu, and D. Wang, “4DRadarSLAM: A 4D Imaging Radar SLAM System for Large-scale Environments based on Pose Graph Optimization,” in *2023 IEEE International Conference on Robotics and Automation (ICRA)*, 2023, pp. 8333–8340.
- [31] Y. Zhuang, B. Wang, J. Huai, and M. Li, “4D iRIOM: 4D Imaging Radar Inertial Odometry and Mapping,” *IEEE Robotics and Automation Letters*, vol. 8, no. 6, pp. 3246–3253, 2023.